

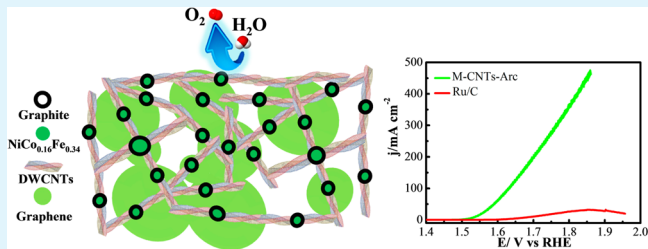
# One-Pot Synthesis of Metal–Carbon Nanotubes Network Hybrids as Highly Efficient Catalysts for Oxygen Evolution Reaction of Water Splitting

Yi Cheng,<sup>†</sup> Chang Liu,<sup>‡</sup> Hui-Ming Cheng,<sup>‡</sup> and San Ping Jiang<sup>\*†</sup>

<sup>†</sup>Fuels and Energy Technology Institute, Curtin University, Perth, Western Australia 6102, Australia

<sup>‡</sup>Shenyang National Laboratory for Materials Science, Institute of Metal Research, Chinese Academy of Sciences, Shenyang 110016, China

**ABSTRACT:** Oxygen evolution reaction (OER) is the most important reaction in hydrogen production from water splitting. Here we developed metal–carbon nanotubes (M-CNTs) hybrids with high metal oxide catalyst loading synthesized by arc-discharge and chemical vapor deposition (CVD) methods as electrocatalysts for OER in alkaline solutions. The M-CNTs hybrids produced by arc-discharge (M-CNTs-Arc) and CVD (M-CNTs-CVD) exhibit a core-shell-like structure, in which metal nanoparticles (NPs) encapsulated by graphite shells are connected by carbon nanotubes (CNTs), forming M-CNTs network hybrids. M-CNTs-Arc has  $\text{NiCo}_{0.16}\text{Fe}_{0.34}$  metal core and shows very high activity and superior stability for OER, achieving  $100 \text{ A g}^{-1}$  at an overpotential ( $\eta$ ) of 0.29 V and  $500 \text{ A g}^{-1}$  at  $\eta = 0.37 \text{ V}$  in 1 M KOH solution. This is probably the highest activity reported for OER in alkaline solutions. The reaction follows the first-order kinetics with respect to  $\text{OH}^-$  concentration and Tafel slope of  $34 \text{ mV dec}^{-1}$ . The results demonstrate a highly efficient, scalable, and low-cost one-step synthesis method for developing highly active and stable catalysts for electrochemical water splitting in alkaline solutions.



**KEYWORDS:** metal–carbon nanotubes hybrids, one-pot synthesis, arc-discharge, chemical vapor deposition, oxygen evolution reaction, alkaline water electrolysis

## 1. INTRODUCTION

Hydrogen production from water splitting driving by renewable energy is an attractive environmental friendly pathway for renewable energy storage. However, the efficiency of the photo- or electrochemical water splitting is greatly constrained by the high overpotentials of oxygen evolution reaction (OER).<sup>1</sup> State-of-the-art OER catalysts such as precious metals based  $\text{RuO}_2$ ,  $\text{IrO}_2$ , and their combination are not economically viable due to their high price and scarcity.<sup>2–6</sup> There are extensive research activities on the metal oxide based materials as electrocatalysts, including nickel, iron, and cobalt based oxides/hydroxides,<sup>3,7–11</sup> spinels,<sup>12</sup> and perovskites.<sup>13,14</sup> The results indicate that high specific surface area is beneficial for the electrochemical activity of OER catalysts. There are various synthesis methods to achieve nanoscaled OER catalysts with high surface area, including electrodeposition,<sup>15–17</sup> sol–gel,<sup>18</sup> solution cast,<sup>11</sup> and hydrothermal precipitation.<sup>19</sup> Metal oxide thin films are also attractive due to the high surface area and high mobility of electrons through the nanometer scale thin-film to reach the supported electrode.<sup>9,20,21</sup> However, large scale fabrication of thin and crack-free film electrodes within a few nanometers is a challenging issue for their practical application.

Another strategy is to incorporate the metal oxides with high surface area and conductive carbon materials. The carbon

material not only can significantly increase the conductivity of the oxides or hydroxides based electrocatalysts but also can enhance the stability of the nanostructured catalysts.<sup>22</sup> Carbon nanotubes (CNTs) and graphene have attracted extensive attention as catalyst supports for OER due to high mechanical strength, excellent electrical conductivities, and chemical stability.<sup>23</sup> Wu et al.<sup>24</sup> prepared  $\text{Co}_2\text{O}_3$  particles supported on single-walled CNTs (SWCNTs) and yielded a current density of  $66 \text{ A g}^{-1}$  at  $\eta = 0.37 \text{ V}$  in 1 M KOH solution, significantly better than unsupported  $\text{Co}_2\text{O}_3$  nanocrystals. Cobalt oxide nanoparticles (NPs) supported on oxidized multiwalled CNTs (MWCNTs) was reported to exhibit an onset potential of 1.51 V vs RHE and a current density of  $10 \text{ mA cm}^{-2}$  ( $40 \text{ A g}^{-1}$ ) at  $\eta = 0.39 \text{ V}$  in 0.1 M KOH.<sup>19</sup>  $\text{Co}_3\text{O}_4$  nanocrystals grown on reduced graphene oxide exhibits a current density of  $10 \text{ mA cm}^{-2}$  ( $10 \text{ A g}^{-1}$ ) at an overpotential of  $\sim 0.31 \text{ V}$  in 1 M KOH solution with catalyst loading of  $1 \text{ mg cm}^{-2}$ .<sup>25</sup> Manganese oxide supported onto CNTs also shows high activity and stability for water splitting in neutral conditions.<sup>26</sup> We showed most recently that graphene supported  $\text{MnO}_2$  nanowires have a

Received: February 19, 2014

Accepted: June 13, 2014

Published: June 13, 2014

much higher electrocatalytic activity for the OER in alkaline solutions than that of Pt/C catalysts.<sup>27</sup> However, preparation of CNT or graphene supported metal oxide catalysts generally involves multisynthesis steps and is difficult to control and scale up.

CNTs are promising supports of metal or metal oxide-based nanostructured electrocatalysts mainly because of their excellent conductivity, ultrahigh surface area, and good chemical, thermal and structural stability.<sup>19,28,29</sup> Chemical vapor deposition and arc-discharge are widely used techniques to grow high quality CNTs with commercially viable quantities.<sup>30–32</sup> For example, as early as in 1998, we demonstrated the synthesis of high quality SWCNTs with a yield of tens of milligrams per batch using a floating catalysts chemical vapor deposition (CVD) method.<sup>33</sup> Industrial-scale production of SWCNTs is also possible using layered double hydroxides as catalysts.<sup>34</sup> The multistep purification process of the as-synthesized CNTs is generally required due to the CNTs inevitably containing carbonaceous impurities (e.g., amorphous carbon, graphite, and carbon nanoparticles) and metal catalyst particles, such as Ni, Fe, and Co.<sup>32</sup> On the other hand, it may be possible to incorporate metal oxide catalysts during the growth of CNTs by the arc-discharge and CVD methods, instantaneously forming electrocatalysts for electrochemical energy conversion and storage applications. Here we report an efficient and scalable synthesis method to fabricate metallic NPs embedded CNTs (M-CNTs) hybrid catalysts by directly growing CNTs on transition metal catalysts using arc-discharge and CVD techniques. The results demonstrate that one-pot synthesized hybrid catalysts have excellent activity and superior stability for OER in alkaline solutions.

## 2. EXPERIMENTAL SECTION

**2.1. One-Pot Synthesis of Metallic NPs Embedded CNTs Hybrids.** The metal–CNT hybrids synthesized by arc-discharge and CVD techniques are denoted as M-CNT-Arc and M-CNT-CVD, respectively. The M-CNT-Arc samples were prepared by a hydrogen arc discharge method, the details are described previously.<sup>35</sup> Briefly, a mixture of 2.6 at. % Ni, 0.7 at. % Fe, 0.7 at. % Co, and graphite powder were used as the anode, hydrogen was used as the buffer gas, and electric arc was operated under a DC mode between the anode and a pure graphite cathode. After discharge for a few minutes, a high yield web-like substance, which consists of CNTs and metallic NPs, was collected between the cathode and the upper chamber wall.

The M-CNT-CVD samples were prepared by a floating catalyst CVD method.<sup>36</sup> Typically, 99 wt % ferrocene and 1 wt % sulfur serve as the catalyst precursor and growth promoter, respectively. They were carried into the reaction zone by 2000 sccm H<sub>2</sub> and 3 sccm CH<sub>4</sub> to grow SWCNTs at 1100 °C; thin films of SWCNTs with metallic NPs embedded were then collected at downstream of the quartz tube reactor.

Metallic NP catalysts embedded in the M-CNTs network hybrids were separated from the CNTs networks by calcinations of M-CNTs-Arc and M-CNTs-CVD at 500 °C for 1 h to decompose the carbon materials. The composition of metal catalysts was analyzed using inductively coupled plasma-optical emission spectrometry (ICP-OES PerkinElmer, Optima 7300 DV). In addition, the metal oxide–CNTs were also prepared by mechanically mixing NiCoFeO<sub>x</sub> and FeO<sub>x</sub> with pure double-walled CNTs (DWCNTs) and single-walled CNTs (SWCNTs), respectively, and the metal oxide loading (MO<sub>x</sub>:CNTs ratio) was kept the same with that of corresponding M-CNTs hybrids. Briefly, 30 mg of DWCNTs was mixed with 35.4 mg of NiCoFeO<sub>x</sub> to form NiCoFeO<sub>x</sub>-DWCNTs catalysts and 30 mg of SWCNTs was mixed with 86 mg of FeO<sub>x</sub> to form FeO<sub>x</sub>-SWCNTs catalysts. The mixtures were ground in a mortar and dispersed in 50 mL of ethanol solution, followed by mixing under ultrasonication treatment for 15

min. The mixed catalysts were filtered and dried at 70 °C in a vacuum oven.

**2.2. Characterization.** Thermogravimetric analysis (TG, Q5000) was conducted to measure the content of carbon materials in the M-CNTs hybrids. Scanning electron microscopy with 5 keV and X-ray energy dispersion spectroscopy with 15 keV (SEM, NEON 40EsB) were applied to examine the microstructure and element distribution of the M-CNTs hybrid. The morphology of the catalysts was characterized using transmission electron microscopy (TEM, JEOL3000) operating at 200 kV. The structure was identified with X-ray diffraction (XRD, Rigaku D/MAX RINT 2500) operated at 40 kV and 30 mA with Cu K $\alpha$  in the range of 20–90°. The Raman spectra were recorded in air at room temperature using a PerkinElmer GX FT-IR/Raman spectrometer with a backscattered configuration and equipped with an Nd:YAG laser at 1064 nm as its light source for Raman.

The electrochemical measurements were conducted in a three electrode cell with a Luggin capillary. The tip of the Luggin capillary was placed 3 mm beneath the working electrode. Generally, 4 mg of the as-prepared catalyst was ultrasonically mixed in a Nafion solution (4 mL, Ethanol:Nafion = 9:1, Nafion 520, DuPont, USA) to form a homogeneous ink. Five microliters of the catalyst ink was pipetted onto the surface of a glassy carbon electrode (GCE) and dried in air. The diameter of the GCE was 5 mm. Without specification, the catalyst loading was 0.025 mg cm<sup>-2</sup>. The ohmic potential drop between the working electrode and the tip of the Luggin capillary was estimated by measuring the electrode resistance at 30 kHz. A Pt wire and saturated calomel electrode (SCE) were used as the counter and reference electrodes, respectively. All potentials in the present study were given versus RHE reference electrode ( $E_{\text{RHE}} = E_{\text{SCE}} + 0.247 + 0.059\text{pH}$ , here 0.247 V is the potential for SCE at 20 °C).

The electrochemically active surface area (ESA) was estimated from the nonfaradaic capacitive current associated with electrochemical double-layer capacitance of the catalytic surface from scan rate dependence of cyclic voltammograms (CVs).<sup>37,38</sup> The CVs were obtained at a scan rate of 10 mV s<sup>-1</sup> in the potential range between -1.5 and +0.6 V (vs SCE). The linear scan voltammetry (LSV) was conducted at a scan rate of 1 mV s<sup>-1</sup> in the potential range between 0 and 1 V (vs SCE) and the system was stabilized after 10 cycles. IR-corrected Tafel plots were recorded at a scan rate of 1 mV s<sup>-1</sup> with the electrode initially conditioned at a potential of 0.65 V (vs SCE) for 5 min before the scan.<sup>39</sup> Chronopotentiometry was conducted at different current densities with catalyst loading of 0.1 mg cm<sup>-2</sup>, using a Gamery Reference 3000 Potentiostat. Except for the measurement of ESA, all the electrochemical tests were conducted on a rotating disk electrode with a rotation rate of 1600 rpm in order to minimize the interference of the bubbles formed at the electrode surface. For comparison, a commercial Ru/C (20 wt % Ru on Vulcan carbon black from Premetek Co.) was also investigated for OER under identical conditions.

The effect of pH on the activity of M-CNTs hybrid catalysts was studied by LSV in KNO<sub>3</sub> solution using scanning rate of 10 mV s<sup>-1</sup> under static conditions. pH of the solution was adjusted with the addition of 1 M KOH or H<sub>2</sub>SO<sub>4</sub> (the ionic strength was kept at 1 M). The pH of the solution was not buffered to avoid influences from the specific adsorption of multivalent anions.<sup>40</sup>

## 3. RESULTS AND DISCUSSION

**3.1. Characterization of M-CNTs Hybrids.** Figure 1 is the TGA curves of the as-synthesized M-CNTs-Arc and M-CNTs-CVD hybrids. The increasing of weight around 350–500 and 200–400 °C for M-CNTs-Arc and M-CNTs-CVD, respectively, is due to the oxidation of metal catalysts. Carbon supports decompose at temperatures around 500–800 °C for M-CNTs-Arc and 350–650 °C for M-CNTs-CVD. The content of carbon supports was estimated to be 45.9 ± 3% in M-CNTs-Arc and 25.8 ± 2.8% in M-CNTs-CVD. This indicates that metal catalyst embedded was 54.1 and 74.2%

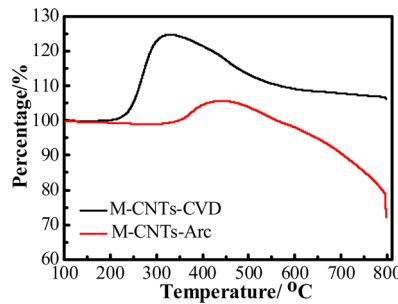


**Figure 1.** TGA curves of M-CNTs-Arc and M-CNTs-CVD hybrid catalysts.

for M-CNTs-Arc and M-CNTs-CVD, respectively. The composition of metal catalysts separated from M-CNTs-Arc as analyzed by ICP consists of  $35.7 \pm 0.2\%$  Ni,  $12.1 \pm 0.15\%$  Fe, and  $5.7 \pm 0.12\%$  Co. Thus, the atomic ratio of Ni:Co:Fe of the metal catalysts in M-CNTs-Arc is 1:0.16:0.34, giving the catalyst formula  $\text{NiCo}_{0.16}\text{Fe}_{0.34}$  in metallic form and  $\text{NiCo}_{0.16}\text{Fe}_{0.34}\text{O}_x$  in oxidized form. In the case of M-CNTs-CVD, as expected, only Fe was detected, indicating the calcinated catalysts is  $\text{FeO}_x$ . The BET surface area of M-CNTs-Arc, M-CNTs-CVD,  $\text{NiCo}_{0.16}\text{Fe}_{0.34}\text{O}_x$ , and  $\text{FeO}_x$  is 166.5, 88.5, 38.3, and  $36.8 \text{ m}^2 \text{ g}^{-1}$ , respectively.

Figure 2 is the SEM and HRTEM micrographs of metal NP embedded CNTs hybrid catalysts. The SEM images indicate that both M-CNTs-Arc and M-CNTs-CVD have a porous structure with a metal particle connected by interconnected CNTs or CNTs bundles (Figure 2A,B). The metal–CNTs hybrids produced by arc-discharge and CVD show an interesting core–shell-like structure, in which metal NPs core is encapsulated by a graphite shell and connected by CNTs network (Figure 2C–F). M-CNTs-Arc exhibits a metal core with an average size  $\sim 6.7 \text{ nm}$  and a 1–3 nm thick graphite or amorphous carbon shell, which is connected mainly by DWCNTs (Figure 2C,D). The diameter of DWCNTs is  $\sim 3 \text{ nm}$  (inset a in Figure 2C). In the case of hybrid catalysts synthesized by CVD, M-CNTs-CVD, and the size of metal core is  $\sim 11.0 \text{ nm}$  surrounded by a 1.5–2.5 nm thick graphite shell (Figure 2E,F). The core–shell structures are mainly connected by SWCNTs with sizes around 2 nm (inset c in Figure 2E). The observation of SWCNTs in M-CNTs-CVD is consistent with a previous study.<sup>41</sup> The  $\text{NiCo}_{0.16}\text{Fe}_{0.34}\text{O}_x$  and  $\text{FeO}_x$  metal oxide catalysts obtained from the M-CNTs hybrids were also characterized by TEM (Figure 2G,H). The average size of the  $\text{NiCo}_{0.16}\text{Fe}_{0.34}\text{O}_x$  metal oxides and  $\text{FeO}_x$  catalysts is 38.2 and 34.8 nm, respectively. The large size of the metal catalysts is mainly due to the sintering and aggregation of the metal catalysts during the decomposition treatment at 500 °C. The EDS spectra confirm the existence of Ni, Fe, and Co for M-CNTs-Arc (Figure 2I), whereas in the case of M-CNTs-CVD, the metal catalysts only contain Fe (Figure 2J).

Figure 3A is the XRD spectra of M-CNTs-Arc and M-CNTs-CVD, as well as the separated metal oxide catalysts. For M-CNTs-Arc, the high intensity peak around 26.5° and 54.7° is from CNTs and graphite. The peaks around 44.1° and 51.3° can be attributed to  $\text{FeNi}_3$ ,  $\text{FeNi}$ , or  $\text{CoFe}$  alloy. In the case of M-CNTs-CVD, the peak at 44.6° is related to metallic Fe, consistent with the EDS analysis. This indicates that M-CNTs-CVD is composed of a metallic Fe nanoparticle core. However, no peak around 26.5° was observed, probably due to the lower content of graphite and CNTs in the sample.  $\text{Fe}_2\text{O}_3$  was

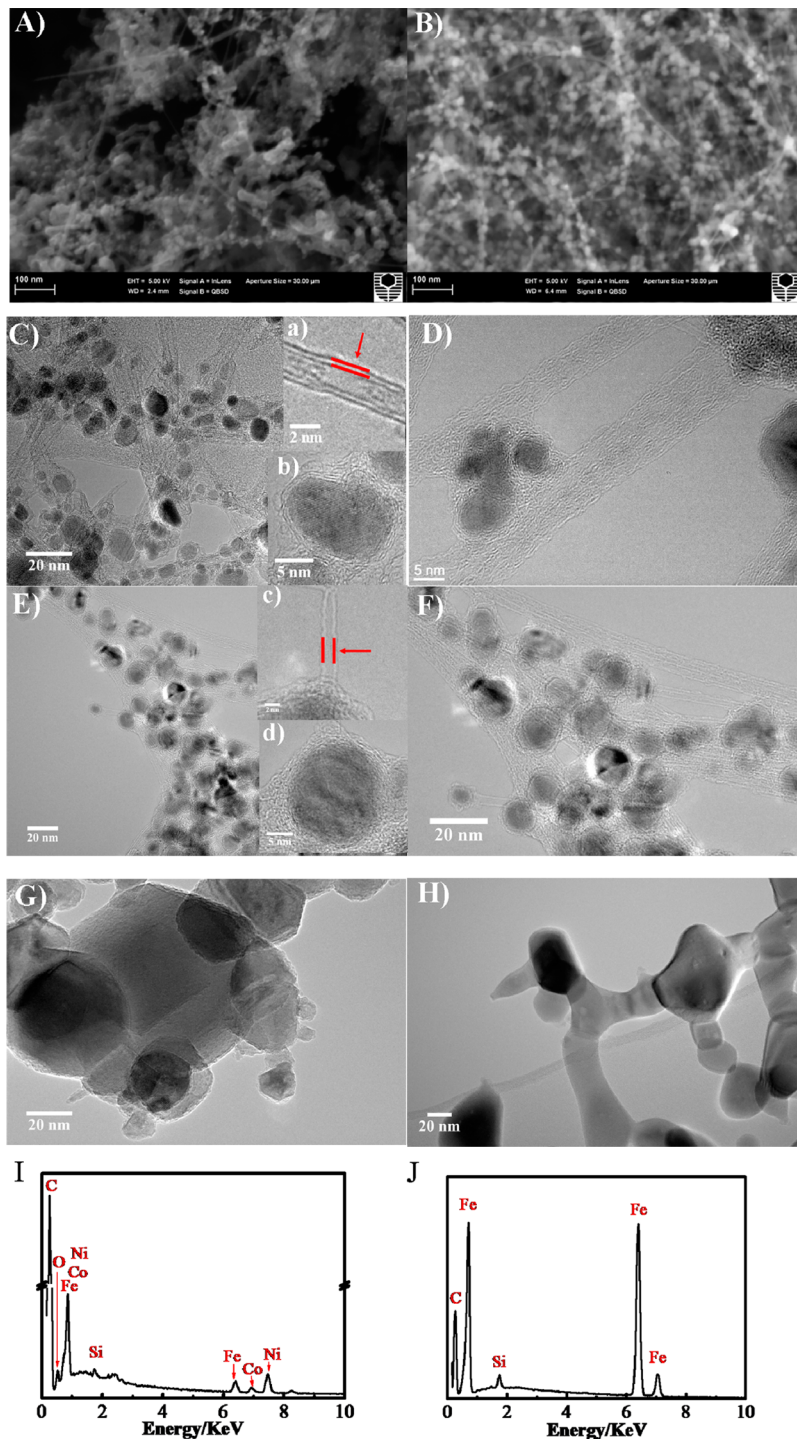
detected after the calcination of M-CNTs-CVD hybrids. The XRD spectra also indicate  $\text{NiCo}_{0.16}\text{Fe}_{0.34}\text{O}_x$  is mainly composed of NiO and  $\text{NiFe}_2\text{O}_4$ . No Co based oxides were detected, probably due to the small amount of cobalt and the formation of alloy with Fe and Ni.

Figure 3B is the Raman spectra obtained from M-CNTs-Arc and M-CNTs-CVD. The peaks around 1270, 1590, and 2540  $\text{cm}^{-1}$  correspond to the D band, G band, and the second order G' band of typical CNTs. The  $I_D/I_G$  is calculated as 1.01 and 0.57 for CNTs produced by arc-discharge and CVD, respectively. In the case of M-CNTs-CVD, the high intensity radial breathing mode (RBM) observed around 100–300  $\text{cm}^{-1}$  is typical for SWCNTs,<sup>42–44</sup> indicating that the encapsulated Fe particles are mainly collected by SWCNTs, consistent with the HRTEM results. However, the largely depressed RBM and increased  $I_D/I_G$  ratio observed for M-CNTs-Arc indicate the presence of DWCNTs<sup>45</sup> between the encapsulated  $\text{NiCo}_{0.16}\text{Fe}_{0.34}$  metal core in the case of M-CNTs-Arc catalysts.

**3.2. Electrochemical Analysis.** Figure 4 is the CV of M-CNTs-Arc, M-CNTs-CVD,  $\text{NiCo}_{0.16}\text{Fe}_{0.34}\text{O}_x$ , and  $\text{FeO}_x$ , measured at scan rate of 10 mV s<sup>-1</sup> in 1 M KOH solution. The catalyst loading was 0.025 mg cm<sup>-2</sup>. In the case of M-CNTs-Arc hybrid catalysts, the oxidation and reduction potential change with the cycling time (Figure 4A). The oxidation peak potential is 1.43 V for the first cycle and decreases to 1.4 V after 11 cycles. And the increase of the area for the redox couple with cycling is attributed to the increasing passivation of  $\text{NiCo}_{0.16}\text{Fe}_{0.34}$  into Ni-based hydroxides and oxyhydroxides during cycling.<sup>7,20,21</sup> The redox potential at 1.4 and 1.3 V is most likely associated with the transformation between  $\text{Ni(OH)}_2$  and  $\text{NiOOH}$  in alkaline electrolyte.<sup>1,20,21,46</sup> Similar to M-CNTs-Arc, the redox potentials of  $\text{NiCo}_{0.16}\text{Fe}_{0.34}\text{O}_x$  redox peaks occur at potentials of 1.4 and 1.32 V. However, the area of the redox reaction of metal oxide is much smaller than that of M-CNTs-Arc due to the smaller surface area and low electronic conductivity.<sup>47</sup> In the case of M-CNTs-CVD, the passivation of metallic Fe to Fe(II)/Fe(III) oxides/hydroxides occur at potential between –0.1 and +0.3 V (Figure 4B).<sup>48,46</sup>

The electrochemically active surface area (ESA) for the M-CNTs hybrid catalysts was estimated from the electrochemical double-layer capacitance ( $C_{DL}$ ) of the catalytic surface (here we use a general specific capacitance  $C_s = 0.040 \text{ mF cm}^{-2}$  to estimate the ESA for carbon proposed by McCrory et al.<sup>37</sup>). The  $C_{DL}$  is calculated based on the plot of  $i_c$  as a function of the scan rate  $\nu$ , yielding a straight line with a slope equal to  $C_{DL}$  ( $i_c = \nu C_{DL}$ ) (Figure 4C). On the basis of the slopes, the ESA is 23.4, 16.4, 5.7, and  $6.0 \text{ m}^2 \text{ g}^{-1}$  for M-CNTs-Arc, M-CNTs-CVD,  $\text{NiCo}_{0.16}\text{Fe}_{0.34}\text{O}_x$ , and  $\text{FeO}_x$ , respectively. The ESA of the catalysts is substantially smaller than the corresponding BET surface area (see Table 1).

**3.3. Electrocatalytic Activity for OER.** Figure 5A is the LSV for OER on M-CNTs-Arc, M-CNTs-CVD,  $\text{NiCo}_{0.16}\text{Fe}_{0.34}\text{O}_x$ ,  $\text{FeO}_x$ , and 20%Ru/C catalysts, measured at scan rate of 1 mV s<sup>-1</sup> in 1 M KOH solutions. The catalyst loading was 0.025 mg cm<sup>-2</sup>. M-CNTs-Arc hybrid catalysts show the best activity for OER. The onset potential of M-CNTs-Arc is 1.48 V, which is 100 and 70 mV lower than that of 20% Ru/C (1.58 V) and M-CNTs-CVD (1.55 V), respectively. The current density measured at 1.7 V ( $\eta = 0.47 \text{ V}$ ) is  $196 \text{ mA cm}^{-2}$  for M-CNTs-Arc, which is 3.6 times of that of M-CNTs-CVD ( $54 \text{ mA cm}^{-2}$ ) and 20 times of 20% Ru/C ( $10 \text{ mA cm}^{-2}$ ). The metal catalysts separated from the M-CNTs hybrids show a



**Figure 2.** SEM images of (A) M-CNTs-Arc and (B) M-CNTs-CVD and TEM images of (C and D) M-CNTs-Arc. The inset shows (a) a DWCNT and (b) metal core with graphite shell, (E and F) M-CNTs-CVD. The inset shows (c) a SWCNT and (d) the metal core with graphite shell. (G)  $\text{NiCo}_{0.16}\text{Fe}_{0.34}\text{O}_x$  and (H)  $\text{FeO}_x$ . EDS spectra of (I) M-CNTs-Arc and (J) M-CNTs-CVD.

much lower activity for OER. The onset potential for OER on  $\text{NiCo}_{0.16}\text{Fe}_{0.34}\text{O}_x$  and  $\text{FeO}_x$  is 1.55 and 1.60 V, respectively, 70 and 50 mV higher than that of the corresponding M-CNTs-Arc and M-CNTs-CVD hybrid catalysts, respectively. The current density at 1.7 V is 18 and  $3.2 \text{ mA cm}^{-2}$  for the reaction on  $\text{NiCo}_{0.16}\text{Fe}_{0.34}\text{O}_x$  and  $\text{FeO}_x$ , much lower than that of the corresponding M-CNTs-Arc and M-CNTs-CVD. The much lower activity of separated metal catalysts is partially due to the

significant sintering and growth of the metallic catalysts during the high temperature decomposition treatment.

To separate the surface area effect from the intrinsic catalytic activity of the hybrid catalysts, we calculated the specific catalysts activity based on the ESA of the catalysts. The ESA specific activity of M-CNTs-Arc, M-CNTs-CVD,  $\text{NiCo}_{0.16}\text{Fe}_{0.34}\text{O}_x$  and  $\text{FeO}_x$  was calculated to be 32.8, 13.4, 11.8, and  $2.2 \text{ mA cm}^{-2}$  at a potential of 1.7 V in 1 M KOH, respectively. This indicates that high electrocatalytic activity of

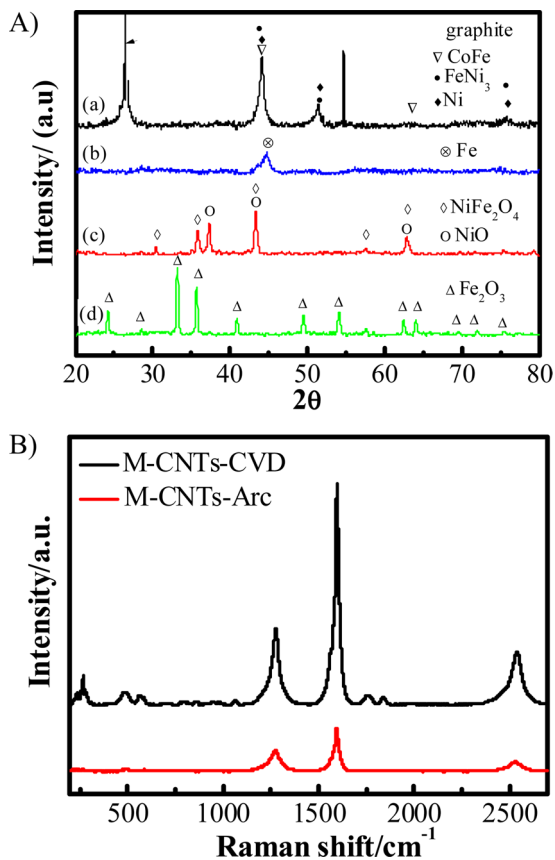


**Figure 3.** (A) XRD patterns of (a) M-CNTs-Arc, (b) M-CNTs-CVD, (c)  $\text{NiCo}_{0.16}\text{Fe}_{0.34}\text{O}_x$ , and (d)  $\text{FeO}_x$ . (B) Raman spectra of M-CNTs-Arc and M-CNTs-CVD.

M-CNTs-Arc and M-CNTs-CVD as compared to the corresponding metal core catalysts is not completely due to the high surface areas of the former.

The electrochemical activity of mechanically mixed  $\text{NiCoFeO}_x$ -DWCNTs and  $\text{FeO}_x$ -SWCNTs were also tested by LSV in 1 M KOH solution under identical conditions, and the results are shown in Figure S8C. The results indicate that the mechanically mixed  $\text{NiCoFeO}_x$ -DWCNTs and  $\text{FeO}_x$ -SWCNTs catalysts show slightly higher electrochemical activity for OER as compared with corresponding  $\text{NiCoFeO}_x$  and  $\text{FeO}_x$  metal catalysts, but still significantly lower than that of one-pot synthesized M-CNTs-Arc and M-CNTs-CVD catalysts. For example, for the reaction on  $\text{NiCoFeO}_x$ -DWCNTs, the onset potential is 1.52 V,  $\sim 30$  mV lower than that on  $\text{NiCo}_{0.16}\text{Fe}_{0.34}\text{O}_x$  but still 40 mV higher than that on M-CNTs-Arc. The current density measured at 1.7 V is  $35 \text{ mA cm}^{-2}$ , about twice of that on  $\text{NiCo}_{0.16}\text{Fe}_{0.34}\text{O}_x$  ( $18 \text{ mA cm}^{-2}$ ); however, it is only 17.8% of  $196 \text{ mA cm}^{-2}$  obtained for the OER on M-CNTs-Arc. The much lower electrocatalytic activity of the mechanically mixed metal oxide-CNTs as compared to the one-pot synthesized M-CNTs hybrids indicates that there might be a synergistic effect between the encapsulated metal catalysts and the interconnected carbon materials including CNTs and graphite. Such a synergistic effect could be responsible for the lower onset potential and significantly higher current density for OER.

Figure 6A shows the chronopotentiometry curves at different current densities for the OER on M-CNTs-Arc, M-CNTs-CVD,  $\text{NiCo}_{0.16}\text{Fe}_{0.34}\text{O}_x$  and  $\text{FeO}_x$  measured in 1 M KOH. The

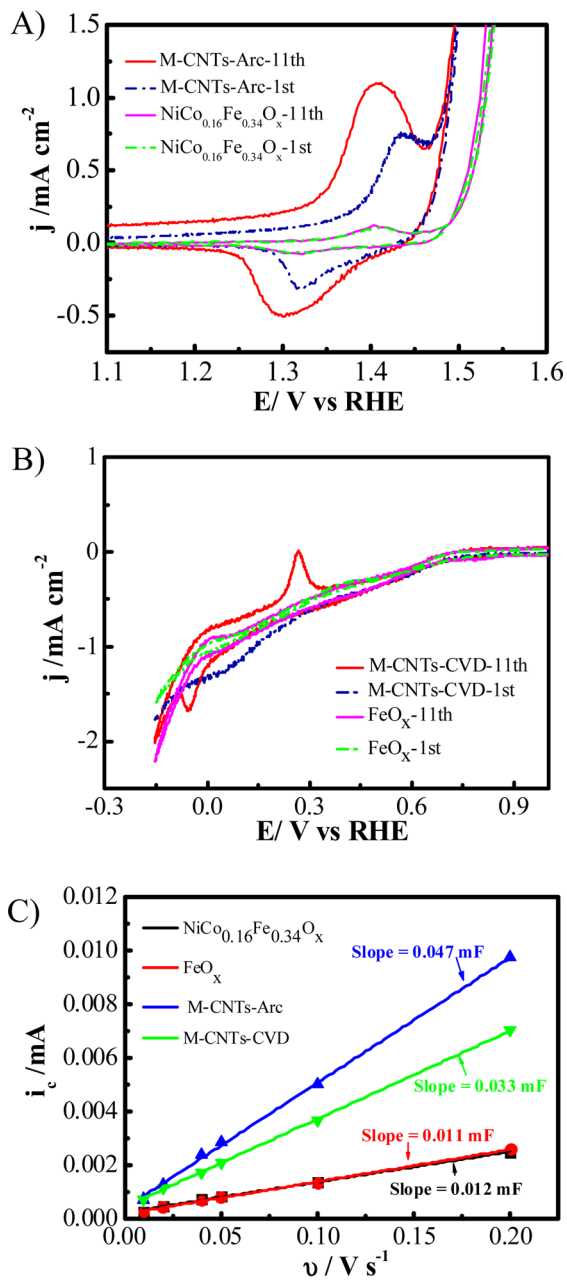


**Figure 4.** Cyclic voltammograms (CV) of (A) M-CNTs-Arc and  $\text{NiCo}_{0.16}\text{Fe}_{0.34}\text{O}_x$  and (B) M-CNTs-CVD and  $\text{FeO}_x$ , measured in 1 M KOH solution with scan rate of  $10 \text{ mV s}^{-1}$  and catalysts loading of  $0.025 \text{ mg cm}^{-2}$  at a rotating rate of 1600 rpm. (C) Anodic charging currents measured at  $-0.05 \text{ V}$  vs SCE plotted as a function of scan rate. The determined double-layer capacitance of the catalysts is taken as the average value of the slope of the linear fits to the data.

catalyst loading was  $0.1 \text{ mg cm}^{-2}$ . The potential to achieve a current density of 2, 5, 10, 20, and  $50 \text{ mA cm}^{-2}$  for M-CNTs-Arc is 1.488, 1.506, 1.524, 1.550, and 1.595 V, respectively. For the reaction on  $\text{NiCo}_{0.16}\text{Fe}_{0.34}\text{O}_x$  the potential at a current density of 2, 5, 10, and  $20 \text{ mA cm}^{-2}$  is 1.596, 1.629, 1.658, and 1.685 V, considerably higher than that observed on M-CNTs-Arc. In the case of M-CNTs-CVD, the potential to achieve 2, 5, 10, 20, and  $50 \text{ mA cm}^{-2}$  is 1.542, 1.581, 1.615, 1.655, and 1.725 V, respectively, higher than that of M-CNTs-Arc under the same current loads. Also, at a current density of  $50 \text{ mA cm}^{-2}$ , the potential for OER on M-CNTs-CVD is not stable; the

**Table 1. Physical and Electrochemical Properties of the Catalysts Materials Studied**

sample	M-CNTs-Arc	M-CNTs-CVD	NiCo <sub>0.16</sub> Fe <sub>0.34</sub> O <sub>x</sub>	FeO <sub>x</sub>	Ru/C
BET surface area ( $\text{m}^2 \text{ g}^{-1}$ )	166.5	88.5	38.3	36.8	
$I_D/I_G$	1.01	0.57			
ESA ( $\text{m}^2 \text{ g}^{-1}$ )	23.4	16.4	5.6	6.0	
onset potential (V)	1.48	1.55	1.55	1.60	1.58
$j_{\text{GEO}, \eta=0.47 \text{ V}} (\text{mA cm}^{-2})$	196	56	18	3.2	8
$j_{\text{ESA}, \eta=0.47 \text{ V}} (\text{mA cm}^{-2})$	32.8	13.4	11.8	2.2	
Tafel slope (mV dec <sup>-1</sup> )	34	34	50	74	50

<sup>#</sup>The onset potential,  $j$ , and Tafel slope measured in 1 M KOH solution with rotating speed of 1600 rpm.  $j_{\text{GEO}}$  is the geometric area based current density and  $j_{\text{ESA}}$  is the specific electrochemically active surface area (ESA) based current density.

potential increased rapidly from 1.725 V to over 2 V after testing for 20 min. This indicates that M-CNTs-CVD hybrids have a much lower stability for OER as compared to M-CNTs-Arc hybrids. In addition, FeO<sub>x</sub> is not able to achieve a current density of 5 mA cm<sup>-2</sup>. This indicates that the electrocatalytic activity of FeO<sub>x</sub> is much lower than that of NiCo<sub>0.16</sub>Fe<sub>0.34</sub>O<sub>x</sub>.

The durability of M-CNTs-Arc, M-CNTs-CVD, and Ru/C for OER was determined using controlled-current electrolysis in 1 M KOH (Figure 6B). The catalyst material was held at a constant current density of 10 mA cm<sup>-2</sup> for 10 h at a rotation rate of 1600 rpm, while the operating potential was measured as a function of time. For M-CNTs-Arc, the potential at 10 mA cm<sup>-2</sup> is 1.52 V ( $\eta = 0.29 \text{ V}$ ) at  $t = 0$ , and the changes in the potential during the stability test are very small. After 10 h of continuous operation, the potential to deliver 10 mA cm<sup>-2</sup> is 1.524 V ( $\eta = 0.294 \text{ V}$ ), very close to the potential before the test. This indicates excellent stability of the M-CNTs-Arc hybrid catalysts. In the case of 20% Ru/C catalysts, the potential to achieve 10 mA cm<sup>-2</sup> is 1.585 V ( $\eta = 0.355 \text{ V}$ ) when  $t = 0$ , increases to 1.625 V ( $\eta = 0.395 \text{ V}$ ) after tested for 5 h and then remains stable around 1.625 V. However, the stability of M-CNTs-CVD hybrids is very poor. The potential to deliver a current density of 10 mA cm<sup>-2</sup> rises from 1.6 V at  $t = 0$  to 1.8 V at  $t = 1 \text{ h}$ . The M-CNTs-CVD is completely decomposed after 2 h of operation and the electrolyte solution turned brownish, most likely due to the dissolution of FeO<sub>x</sub>. The outstanding stability of the M-CNTs-Arc was also further confirmed by polarization at a current density of 50 mA cm<sup>-2</sup> in 1 M KOH. The results show that the potential to achieve 50 mA cm<sup>-2</sup> (500 A g<sup>-1</sup>) is 1.595 V ( $\eta = 0.365 \text{ V}$ ) and the potential remained the same after tested for 10 h, indicating that the M-CNTs-Arc is also very stable at high current densities.

McCrory et al. recently studied the benchmarking heterogeneous electrocatalysts prepared by electrodeposition for OER in 1 M KOH with a rotating rate of 1600 rpm.<sup>37</sup> The overpotentials for achieving a current density of 10 mA cm<sup>-2</sup> for IrO<sub>x</sub>, NiFeO<sub>x</sub>, CoFeO<sub>x</sub>, NiCoO<sub>x</sub>, CoO<sub>x</sub>, NiLaO<sub>x</sub>, NiCuO<sub>x</sub>, NiO<sub>x</sub>, and NiCeO<sub>x</sub> films are 0.32, 0.35, 0.37, 0.38, 0.39, 0.41, 0.41, 0.42, and 0.43 V, respectively. Liang et al. showed that Co<sub>3</sub>O<sub>4</sub> nanocrystals grown on reduced graphene oxide (Co<sub>3</sub>O<sub>4</sub>/N-rmGO) exhibit a current density of 10 mA cm<sup>-2</sup> (or 1 A g<sup>-1</sup>) at  $\eta = \sim 0.31 \text{ V}$  in 1 M KOH solution with catalyst

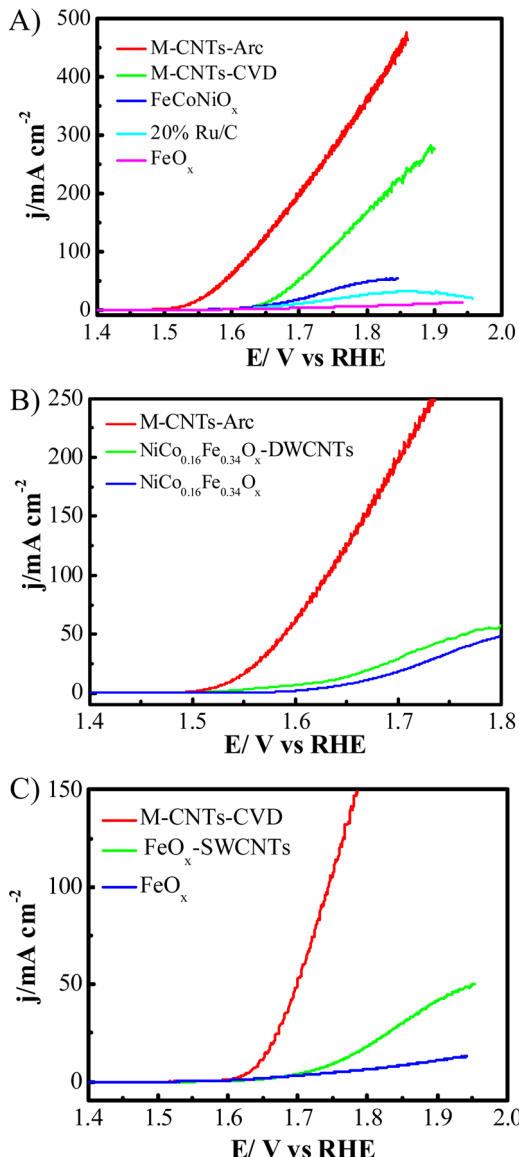


**Figure 5.** Linear scan voltammograms (LSV) of (A) M-CNTs-Arc, M-CNTs-CVD, NiCo<sub>0.16</sub>Fe<sub>0.34</sub>O<sub>x</sub>, FeO<sub>x</sub>, and Ru/C, (B) M-CNTs-Arc, NiCo<sub>0.16</sub>Fe<sub>0.34</sub>O<sub>x</sub>-DWCNTs and NiCo<sub>0.16</sub>Fe<sub>0.34</sub>O<sub>x</sub>, and (C) M-CNTs-CVD, FeO<sub>x</sub>-SWCNTs, and FeO<sub>x</sub>. The LSV was measured in 1 M KOH solution with a scan rate of 1 mV s<sup>-1</sup> and catalyst loading of 0.025 mg cm<sup>-2</sup> at a rotating rate of 1600 rpm.

loading of 1 mg cm<sup>-2</sup>.<sup>25</sup> Ultrathin nickel–iron layered double hydroxide nanoplates supported on oxidized multiwalled carbon nanotubes (MWCNTs) was reported to achieve a current density of 10 A g<sup>-1</sup> at  $\eta = 0.228 \text{ V}$  in 1 M KOH with catalysts loading of 0.25 mg cm<sup>-2</sup>.<sup>11</sup> In the present study, the M-CNTs-Arc hybrid catalyst achieved a current density of 10 mA cm<sup>-2</sup> (or 100 A g<sup>-1</sup>) at  $\eta = 0.29 \text{ V}$  (i.e., 1.524 V vs RHE) in 1 M KOH with catalyst loading of 0.1 mg cm<sup>-2</sup>. This indicates that M-CNTs-Arc hybrids are among the most active nonprecious metal OER catalysts. The results demonstrate that M-CNTs hybrid produced by the arc-discharge technique using NiCo<sub>0.16</sub>Fe<sub>0.34</sub> metal catalysts is a promising catalyst with high activity and superior long-term stability for OER in alkaline solutions.

**3.4. Effect of pH.** The activity of M-CNTs for OER has been found to be critically related to the pH of the solution.

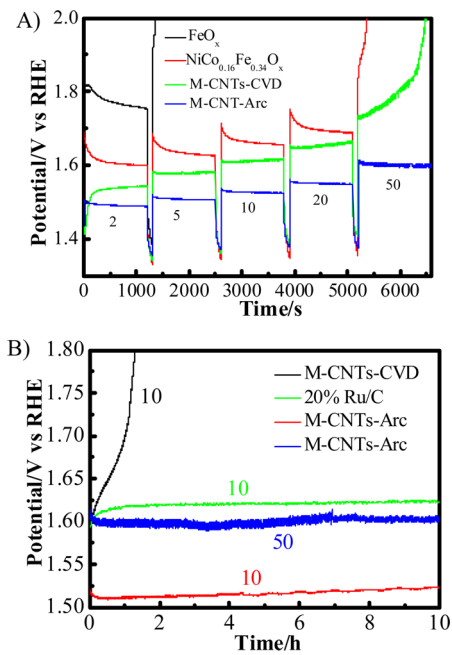


**Figure 6.** (A) Chronopotentiometry of M-CNTs-Arc, M-CNTs-CVD,  $\text{NiCo}_{0.16}\text{Fe}_{0.34}\text{O}_x$ , and  $\text{FeO}_x$ . (B) Stability plots, measured at current densities of 10 and 50  $\text{mA cm}^{-2}$ . The measurements were carried out in 1 M KOH solution with catalyst loading of  $0.1 \text{ mg cm}^{-2}$  and the rotating rate of 1600 rpm. Numbers are current density in  $\text{mA cm}^{-2}$ .

Figure 7 shows the effect of pH on the OER activity for M-CNTs-Arc and M-CNTs-CVD. The variation trend for the onset potential and current density for M-CNTs-CVD and M-CNTs-Arc with pH is similar. The onset potentials for OER on M-CNTs-CVD and M-CNTs-Arc hybrids electrodes increased from  $\sim 1.7$  V at pH = 2.11 to  $\sim 2.2$  V at pH = 10, then decreased sharply to  $\sim 1.5$  V when the pH was above 11 (Figure

7C). The current densities of M-CNTs measured at 1.7 V are low in the pH range of 1–10. However, a dramatic increase were observed when pH increased to 12–14, reaching current density of 180 and 55  $\text{mA cm}^{-2}$  at pH = 13.6 for M-CNTs-CVD and M-CNTs-Arc, respectively (Figure 7D). The different behavior of M-CNTs as a function of pH of the electrolytes indicates that fundamentally different mechanisms exist for OER under acidic, neutral, and basic conditions. The reason for such drastic change of the reaction activity of the M-CNTs hybrid catalysts for OER as a function of solution pH is not clear at this stage. One possible reason may be related to the significant role of the surface electrochemistry of hydrous oxide, formed in acidic, neutral, and basic conditions on the electrodes of transition metals due to their amphoteric nature.<sup>7,8,49</sup> Takashima et al. found that the OER overpotential for manganese oxide increased from 0.5 to 0.7 V when the pH increased from 4 to 8, but sharply decreased to 0.48 V at pH  $\geq 9$ , and proposed that the pH dependence of onset potential and current density might be due to the surface charge caused by  $\text{OH}^-$  species.<sup>50</sup> At low pH, the M-CNTs-Arc and M-CNTs-CVD are protonated and thus positively charged. At high pH, they would act as acids, adsorbing  $\text{OH}^-$  or donating protons and thus becoming negatively charged. Lower onset potentials are expected in basic solutions than in acidic/neutral solutions because the highly charged metal ions with excess hydroxide ions are active sites for oxygen evolution and for oxygen species such as  $\text{M-O}^-$ , it is easier to donate electrons in alkaline solutions than in acid or neutral solutions with positively charged species.<sup>50</sup>

Figure 8 is the Tafel slope plots for OER on M-CNTs-Arc and M-CNTs-CVD hybrids, measured in 1 M KOH solution at a scanning rate of 1  $\text{mV s}^{-1}$ . The Tafel slope of M-CNTs-Arc is 34  $\text{mV dec}^{-1}$ , lower than 50  $\text{mV dec}^{-1}$  obtained on the  $\text{NiCo}_{0.16}\text{Fe}_{0.34}\text{O}_x$  metal catalysts (Figure 8A). For the OER on hydrous  $\text{NiO}$ , Lyons et al. reported the Tafel slope of 40–60  $\text{mV dec}^{-1}$  at low overpotentials.<sup>8,51</sup> In the case of M-CNTs-

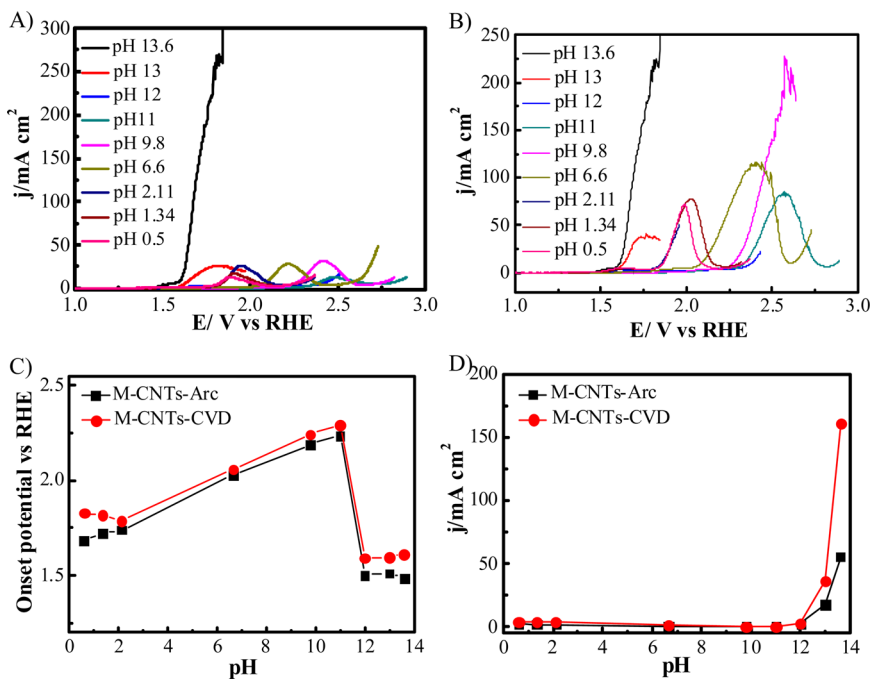


**Figure 7.** Linear scan voltammetry of (A) M-CNTs-Arc and (B) M-CNTs-CVD under different pH solutions for OER, measured at scan rate of 10  $\text{mV s}^{-1}$ . (C) Plots of onset potential as a function of pH. (D) Plots of current density measured at 1.7 V vs RHE as a function of pH.

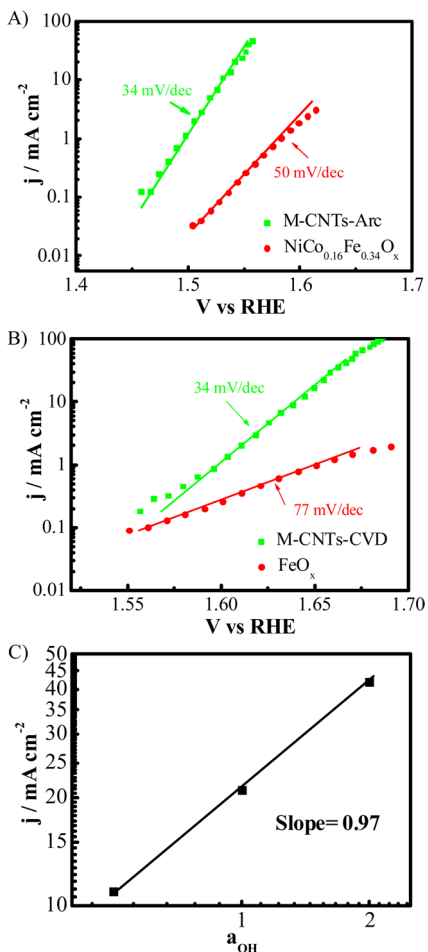


**Figure 8.** Tafel plots for oxygen evolution in 1 M KOH solutions at (A) M-CNTs-Arc and NiCo<sub>0.16</sub>Fe<sub>0.34</sub>O<sub>x</sub> and (B) M-CNTs-CVD and FeO<sub>x</sub>. (C) Plots of reaction order for OER on M-CNTs-Arc.

CVD, the Tafel slope is 34 mV dec<sup>-1</sup>, also lower than 77 mV dec<sup>-1</sup> measured on FeO<sub>x</sub>. The lower Tafel slopes observed on M-CNTs as compared to that on metal oxide catalysts indicate an increased electron transfer for OER,<sup>11,20,21</sup> an indication of the synergistic effect of graphitic shell and CNTs network on the electrocatalytic activity of metal NPs catalyst. The reaction order plots with respect to OH<sup>-</sup> activity ( $\log I$  vs  $\log a_{\text{OH}}^{-1}$  at a given value) of M-CNTs-Arc were also constructed based on the polarization data in 0.5, 1, and 2 M KOH solution (Figure 8C). A reaction order of 0.97 was obtained, indicating that the OER follows a first-order kinetics with respect to the OH<sup>-</sup> concentration. However, the reaction order was not obtained for M-CNTs-CVD because of the poor stability of the catalysts, which results in the nonlinear function of  $\log I$  and  $\log a_{\text{OH}}^{-1}$ .

The Tafel slopes of M-CNTs for OER were also measured in 1, 0.1, and 0.01 M KOH solutions and the results are shown in Figure 9. For M-CNTs-Arc, the Tafel slope recorded is 74 mV dec<sup>-1</sup> in 0.01 M KOH solution. However, the Tafel slope is decreased to ~34 mV dec<sup>-1</sup> when the concentration of KOH of solution is in the range of 0.1–1 M KOH. In the case of M-CNTs-CVD, a Tafel slope of 34, 41, and 89 mV dec<sup>-1</sup> was obtained in 1, 0.1, and 0.01 M KOH solutions, respectively, indicating that the rate-determining step is influenced by the concentration of KOH.

The significant dependence of OER activity on pH demonstrates that OH<sup>-</sup> is playing a critical role in OER on

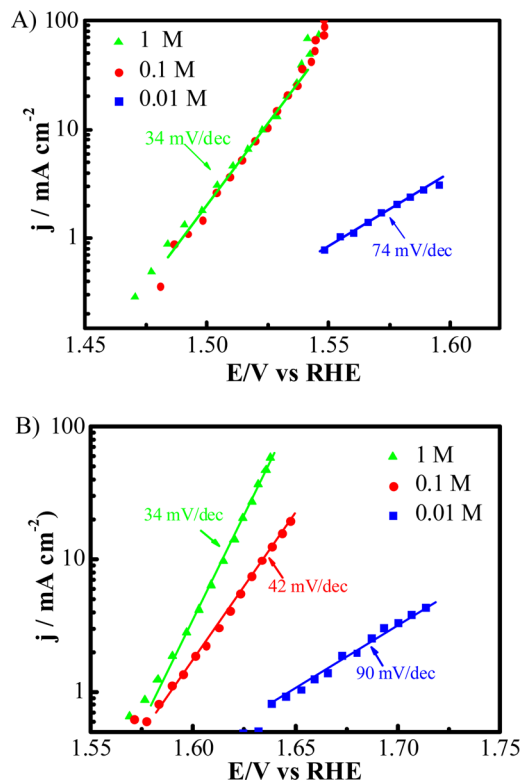


**Figure 9.** Tafel plots for oxygen evolution reaction at (A) M-CNTs-Arc and (B) M-CNTs-CVD catalysts measured in 1, 0.1, and 0.01 M KOH solutions.

M-CNTs hybrid catalysts. As shown in Figure 3A, the transformation of NiCo<sub>0.16</sub>Fe<sub>0.34</sub> into NiCo<sub>0.16</sub>Fe<sub>0.34</sub>-OOH (M-OOH) occurs before the oxygen evolution reaction. Thus, the initial steps of OER could be the absorption of OH<sup>-</sup> on M-CNTs-Arc, forming M-CNTs-NiCo<sub>0.16</sub>Fe<sub>0.34</sub>-OOH.<sup>8,46</sup> The surface-enhanced Raman spectroscopy also provides evidence of the formation of MOOH intermediates for Ni<sup>52</sup> and NiFe oxides.<sup>20</sup> A Tafel slope of 34 mV dec<sup>-1</sup> with a reaction order of ~1.0 for M-CNTs-Arc indicates that oxygen evolution on M-OOH begins with absorbing OH<sup>-</sup> as a fast step and the subsequent electrochemical interaction between the surface adsorbed intermediate and OH<sup>-</sup>.<sup>46,48</sup> The rate-determining step is most likely the formation of metal oxide or metal oxo species, as shown by Lyons et al.<sup>46,48,51</sup>

The superiority of M-CNTs-Arc hybrid catalysts can be attributed to the following reasons. First, NiCo<sub>0.16</sub>Fe<sub>0.34</sub> and its oxides are superior catalysts for OER as compared with that of Fe and FeO<sub>x</sub> in the case of M-CNTs-CVD. Second, the M-CNTs hybrids produced by arc-discharge using NiCo<sub>0.16</sub>Fe<sub>0.34</sub> catalysts are connected mainly by DWCNTs networks, and the encapsulated NiCo<sub>0.16</sub>Fe<sub>0.34</sub> with graphite enhances the activity and stability for OER. For M-CNTs-CVD, metal catalysts are interconnected via SWCNTs networks, which generally contains large amount of semiconductor.<sup>53–55</sup> The excellent conductivity of DWCNTs would provide a better path way for electron charge transfer during OER, as compared to SWCNTs.

#### 4. CONCLUSION

Here we, for the first time, reported a simple, scalable, and one-pot synthesis method to fabricate metal–CNTs network hybrid catalysts using conventional arc-discharge and CVD techniques for OER of water electrolysis. The metal–CNTs hybrids

synthesized by the arc-discharge technique with  $\text{NiCo}_{0.16}\text{Fe}_{0.34}$  catalysts (M-CNTs-Arc) and the CVD technique with Fe catalysts (M-CNTs-CVD) have significantly higher electrocatalytic activity for OER in alkaline solutions as compared with bare metal oxides or CNTs-supported metal oxide catalysts. The as-synthesized M-CNTs-Arc catalysts show a low onset potential (1.48 V), significantly high activity, and super stability for OER. The M-CNTs-Arc hybrids produced the highest activity for OER in alkaline solutions, achieving  $100 \text{ A g}^{-1}$  at  $\eta = 0.29 \text{ V}$ , and  $500 \text{ A g}^{-1}$  at  $\eta = 0.37 \text{ V}$ . And the Tafel slope of  $34 \text{ mV dec}^{-1}$  with a reaction order of  $\sim 1.0$  for M-CNTs-Arc indicates that oxygen evolution on M-CNTs-Arc is mainly limited by the formation of metal oxide or metal oxo species. The excellent activity and durability of the M-CNTs-Arc network hybrids is most likely due to the synergistic effect between the encapsulated metal catalysts and the interconnected CNTs. The one-pot synthesis techniques show a promising potential for the development of highly active electrocatalysts for OER of water splitting.

## AUTHOR INFORMATION

### Corresponding Author

\*S.P. Jiang. E-mail: S.Jiang@curtin.edu.au.

### Notes

The authors declare no competing financial interest.

## ACKNOWLEDGMENTS

We acknowledge Mr. Jin Zhang for the measurement of the BET surface area of M-CNTs hybrids and Mr. Lei Zhang for the assistance of ICP operation. The project is supported by the Australian Research Council Discovery Project funding scheme (project number: DP120104932). The authors also acknowledge the facilities and the scientific and technical assistance of the Australian Microscopy & Microanalysis Research Facility at the Centre for Microscopy, Characterisation & Analysis, and the University of Western Australia, a facility funded by the University, State, and Commonwealth Governments.

## REFERENCES

- (1) Surendranath, Y.; Nocera, D. G. Oxygen Evolution Reaction Chemistry of Oxide-Based Electrodes. In *Prog. Inorg. Chem.*; John Wiley & Sons, Inc.: New York, 2011; pp 505–560.
- (2) Ursua, A.; Gandia, L. M.; Sanchis, P. Hydrogen Production From Water Electrolysis: Current Status and Future Trends. *Proc. IEEE* **2012**, *100*, 410–426.
- (3) Pletcher, D.; Li, X. Prospects for alkaline zero gap water electrolyzers for hydrogen production. *Int. J. Hydrogen Energy* **2011**, *36*, 15089–15104.
- (4) Fang, Y.-H.; Liu, Z.-P. Mechanism and Tafel Lines of Electro-Oxidation of Water to Oxygen on  $\text{RuO}_2(110)$ . *J. Am. Chem. Soc.* **2010**, *132*, 18214–18222.
- (5) Lyons, M. E. G.; Burke, L. D. Mechanism of oxygen reactions at porous oxide electrodes. Part 1.-Oxygen evolution at  $\text{RuO}_2$  and  $\text{RuSn1-xO}_2$  electrodes in alkaline solution under vigorous electrolysis conditions. *J. Chem. Soc., Faraday Trans. 1* **1987**, *83*, 299–321.
- (6) Lyons, M. E. G.; Floquet, S. Mechanism of oxygen reactions at porous oxide electrodes. Part 2-Oxygen evolution at  $\text{RuO}_2$ ,  $\text{IrO}_2$  and  $\text{Ir}_{x}\text{Ru}_{1-x}\text{O}_2$  electrodes in aqueous acid and alkaline solution. *Phys. Chem. Chem. Phys.* **2011**, *13*, 5314–5335.
- (7) Lyons, M. E. G.; Brandon, M. P. The Oxygen Evolution Reaction on Passive Oxide Covered Transition Metal Electrodes in Alkaline Solution Part II - Cobalt. *Int. J. Electrochem. Sci.* **2008**, *3*, 1425–1462.
- (8) Lyons, M. E. G.; Brandon, M. P. The Oxygen Evolution Reaction on Passive Oxide Covered Transition Metal Electrodes in Aqueous Alkaline Solution. Part 1-Nickel. *Int. J. Electrochem. Sci.* **2008**, *3*, 1386–1424.
- (9) Trotochaud, L.; Ranney, J. K.; Williams, K. N.; Boettcher, S. W. Solution-Cast Metal Oxide Thin Film Electrocatalysts for Oxygen Evolution. *J. Am. Chem. Soc.* **2012**, *134*, 17253–17261.
- (10) Cibrel, D.; Jankulovska, M.; Lana-Villarreal, T.; Gomez, R. Oxygen Evolution at ultrathin nanostructured  $\text{Ni(OH)}_2$  layers deposited on conducting glass. *Int. J. Hydrogen Energy* **2013**, *38*, 2746–2753.
- (11) Gong, M.; Li, Y.; Wang, H.; Liang, Y.; Wu, J. Z.; Zhou, J.; Wang, J.; Regier, T.; Wei, F.; Dai, H. An Advanced Ni–Fe Layered Double Hydroxide Electrocatalyst for Water Oxidation. *J. Am. Chem. Soc.* **2013**, *135*, 8452–8455.
- (12) Hamdani, M.; Singh, R. N.; Chartier, P.  $\text{Co}_3\text{O}_4$  and Co- Based Spinel Oxides Bifunctional Oxygen Electrodes. *Int. J. Electrochem. Sci.* **2010**, *5*, 556–577.
- (13) Bockris, J. O.; Otagawa, T. Mechanism of Oxygen Evolution on Perovskites. *J. Phys. Chem.* **1983**, *87*, 2960–2971.
- (14) Jain, A. N.; Tiwari, S. K.; Singh, R. N.; Chartier, P. Low-Temperature Synthesis of Perovskite-Type Oxides of Lanthanum and Cobalt and Their Electrocatalytic Properties for Oxygen Evolution in Alkaline Solutions. *J. Chem. Soc., Faraday Trans.* **1995**, *91*, 1871–1875.
- (15) Castro, E. B.; Gervasi, C. A. Electrodeposited Ni–Co-Oxide Electrodes: Characterization and Kinetics of the Oxygen Evolution Reaction. *Int. J. Hydrogen Energy* **2000**, *25*, 1163–1170.
- (16) Castro, E. B.; Gervasi, C. A.; Vilche, J. R. Oxygen Evolution on Electrodeposited Cobalt Oxides. *J. Appl. Electrochem.* **1998**, *28*, 835–841.
- (17) Merrill, M. D.; Dougherty, R. C. Metal Oxide Catalysts for the Evolution of  $\text{O}_2$  from  $\text{H}_2\text{O}$ . *J. Phys. Chem. C* **2008**, *112*, 3655–3666.
- (18) Lee, Y.; Suntivich, J.; May, K. J.; Perry, E. E.; Shao-Horn, Y. Synthesis and Activities of Rutile  $\text{IrO}_2$  and  $\text{RuO}_2$  Nanoparticles for Oxygen Evolution in Acid and Alkaline Solutions. *J. Phys. Chem. Lett.* **2012**, *3*, 399–404.
- (19) Lu, X.; Zhao, C. Highly Efficient and Robust Oxygen Evolution Catalysts Achieved by Anchoring Nanocrystalline Cobalt Oxides onto Mildly Oxidized Multiwalled Carbon Nanotubes. *J. Mater. Chem. A* **2013**, *1*, 12053–12059.
- (20) Louie, M. W.; Bell, A. T. An Investigation of Thin-Film Ni–Fe Oxide Catalysts for the Electrochemical Evolution of Oxygen. *J. Am. Chem. Soc.* **2013**, *135*, 12329–12337.
- (21) Smith, R. D. L.; Prévôt, M. S.; Fagan, R. D.; Trudel, S.; Berlinguette, C. P. Water Oxidation Catalysis: Electrocatalytic Response to Metal Stoichiometry in Amorphous Metal Oxide Films Containing Iron, Cobalt, and Nickel. *J. Am. Chem. Soc.* **2013**, *135*, 11580–11586.
- (22) Zou, X.; Su, J.; Silva, R.; Goswami, A.; Sathe, B. R.; Asefa, T. Efficient Oxygen Evolution Reaction Catalyzed by Low-Density Ni-Doped  $\text{Co}_3\text{O}_4$  Nanomaterials Derived from Metal-Embedded Graphitic  $\text{C}_3\text{N}_4$ . *Chem. Commun.* **2013**, *49*, 7522–7524.
- (23) Liu, Q.; Jin, J. T.; Zhang, J. Y.  $\text{NiCO}_2\text{S}_4@\text{graphene}$  as a Bifunctional Electrocatalyst for Oxygen Reduction and Evolution Reactions. *ACS Appl. Mater. Interfaces* **2013**, *5*, 5002–5008.
- (24) Wu, J.; Xue, Y.; Yan, X.; Yan, W.; Cheng, Q.; Xie, Y.  $\text{Co}_3\text{O}_4$  Nanocrystals on Single-Walled Carbon Nanotubes as a Highly Efficient Oxygen-Evolving Catalyst. *Nano Res.* **2012**, *5*, 521–530.
- (25) Liang, Y.; Li, Y.; Wang, H.; Zhou, J.; Wang, J.; Regier, T.; Dai, H.  $\text{Co}_3\text{O}_4$  Nanocrystals on Graphene as a Synergistic Catalyst for Oxygen Reduction Reaction. *Nat. Mater.* **2011**, *10*, 780–786.
- (26) Mette, K.; Bergmann, A.; Tessonnier, J.-P.; Hävecker, M.; Yao, L.; Ressler, T.; Schlögl, R.; Strasser, P.; Behrens, M. Nanostructured Manganese Oxide Supported on Carbon Nanotubes for Electrocatalytic Water Splitting. *ChemCatChem* **2012**, *4*, 851–862.
- (27) Yuan, W. Y.; Shen, P. K.; Jiang, S. P. Controllable Synthesis of Graphene Supported  $\text{MnO}_2$  Nanowires via Self-Assembly for Enhanced Water Oxidation in Both Alkaline and Neutral Solutions. *J. Mater. Chem. A* **2014**, *2*, 123–129.

- (28) Guldi, D. M.; Rahman, G. M. A.; Sgobba, V.; Ehli, C. Multifunctional Molecular Carbon Materials—from Fullerenes to Carbon Nanotubes. *Chem. Soc. Rev.* **2006**, *35*, 471–487.
- (29) Zhang, W.; Sherrell, P.; Minett, A. I.; Razal, J. M.; Chen, J. Carbon Nanotube Architectures As Catalyst Supports for Proton Exchange Membrane Fuel Cells. *Energy Environ. Sci.* **2010**, *3*, 1286–1293.
- (30) Prasek, J.; Drbohlavova, J.; Chomoucka, J.; Hubalek, J.; Jasek, O.; Adam, V.; Kizek, R. Methods for Carbon Nanotubes Synthesis—Review. *J. Mater. Chem.* **2011**, *21*, 15872–15884.
- (31) Liu, C.; Cheng, H. M. Carbon Nanotubes: Controlled Growth and Application. *Mater. Today* **2013**, *16*, 19–28.
- (32) Zhang, Q.; Huang, J.-Q.; Qian, W.-Z.; Zhang, Y.-Y.; Wei, F. The Road for Nanomaterials Industry: A Review of Carbon Nanotube Production, Post-Treatment, and Bulk Applications for Composites and Energy Storage. *Small* **2013**, *9*, 1237–1265.
- (33) Cheng, H. M.; Li, F.; Su, G.; Pan, H. Y.; He, L. L.; Sun, X.; Dresselhaus, M. S. Large-Scale and Low-Cost Synthesis of Single-Walled Carbon Nanotubes by the Catalytic Pyrolysis of Hydrocarbons. *Appl. Phys. Lett.* **1998**, *72*, 3282–3284.
- (34) Zhao, M. Q.; Zhang, Q.; Jia, X. L.; Huang, J. Q.; Zhang, Y. H.; Wei, F. Hierarchical Composites of Single/Double-Walled Carbon Nanotubes Interlinked Flakes from Direct Carbon Deposition on Layered Double Hydroxides. *Adv. Funct. Mater.* **2010**, *20*, 677–685.
- (35) Liu, C.; Cong, H. T.; Li, F.; Tan, P. H.; Cheng, H. M.; Lu, K.; Zhou, B. L. Semi-Continuous Synthesis of Single-Walled Carbon Nanotubes by a Hydrogen Arc Discharge Method. *Carbon* **1999**, *37*, 1865–1868.
- (36) Yu, B.; Liu, C.; Hou, P. X.; Tian, Y.; Li, S. S.; Liu, B. L.; Li, F.; Kauppinen, E. I.; Cheng, H. M. Bulk Synthesis of Large Diameter Semiconducting Single-Walled Carbon Nanotubes by Oxygen-Assisted Floating Catalyst Chemical Vapor Deposition. *J. Am. Chem. Soc.* **2011**, *133*, 5232–5235.
- (37) McCrory, C. C. L.; Jung, S.; Peters, J. C.; Jaramillo, T. F. Benchmarking Heterogeneous Electrocatalysts for the Oxygen Evolution Reaction. *J. Am. Chem. Soc.* **2013**, *135*, 16977–16987.
- (38) Benck, J. D.; Chen, Z.; Kuritzky, L. Y.; Forman, A. J.; Jaramillo, T. F. Amorphous Molybdenum Sulfide Catalysts for Electrochemical Hydrogen Production: Insights into the Origin of their Catalytic Activity. *ACS Catal.* **2012**, *2*, 1916–1923.
- (39) Bediako, D. K.; Surendranath, Y.; Nocera, D. G. Mechanistic Studies of the Oxygen Evolution Reaction Mediated by a Nickel–Borate Thin Film Electrocatalyst. *J. Am. Chem. Soc.* **2013**, *135*, 3662–3674.
- (40) Imanishi, A.; Okamura, T.; Ohashi, N.; Nakamura, R.; Nakato, Y. Mechanism of Water Photooxidation Reaction at Atomically Flat TiO<sub>2</sub> (Rutile) (110) and (100) Surfaces: Dependence on Solution pH. *J. Am. Chem. Soc.* **2007**, *129*, 11569–11578.
- (41) Yu, B.; Liu, C.; Hou, P.-X.; Tian, Y.; Li, S.; Liu, B.; Li, F.; Kauppinen, E. I.; Cheng, H.-M. Bulk Synthesis of Large Diameter Semiconducting Single-Walled Carbon Nanotubes by Oxygen-Assisted Floating Catalyst Chemical Vapor Deposition. *J. Am. Chem. Soc.* **2011**, *133*, 5232–5235.
- (42) Kim, U. J.; Furtado, C. A.; Liu, X. M.; Chen, G. G.; Eklund, P. C. Raman and IR Spectroscopy of Chemically Processed Single-Walled Carbon Nanotubes. *J. Am. Chem. Soc.* **2005**, *127*, 15437–15445.
- (43) Dresselhaus, M. S.; Dresselhaus, G.; Saito, R.; Jorio, A. Raman Spectroscopy of Carbon Nanotubes. In *Carbon Nanotubes: Quantum Cylinders of Graphene*; Saito, S., Zettl, A., Eds.; Elsevier Science Bv: Amsterdam, 2008; pp 83–108.
- (44) Saito, R.; Hofmann, M.; Dresselhaus, G.; Jorio, A.; Dresselhaus, M. S. Raman Spectroscopy of Graphene and Carbon Nanotubes. *Adv. Phys.* **2011**, *60*, 413–550.
- (45) Fujisawa, K.; Komiyama, K.; Muramatsu, H.; Shimamoto, D.; Tojo, T.; Kim, Y. A.; Hayashi, T.; Endo, M.; Oshida, K.; Terrones, M.; Dresselhaus, M. S. Chirality-Dependent Transport in Double-Walled Carbon Nanotube Assemblies: The Role of Inner Tubes. *ACS Nano* **2011**, *5*, 7547–7554.
- (46) Doyle, R. L.; Godwin, I. J.; Brandon, M. P.; Lyons, M. E. G. Redox and Electrochemical Water Splitting Catalytic Properties of Hydrated Metal Oxide Modified Electrodes. *Phys. Chem. Chem. Phys.* **2013**, *15*, 13737–13783.
- (47) Rakhi, R. B.; Chen, W.; Cha, D.; Alshareef, H. N. Nanostructured Ternary Electrodes for Energy-Storage Applications. *Adv. Energy Mater.* **2012**, *2*, 381–389.
- (48) Doyle, R. L.; Lyons, M. E. G. Kinetics and Mechanistic Aspects of the Oxygen Evolution Reaction at Hydrous Iron Oxide Films in Base. *J. Electrochem. Soc.* **2013**, *160*, H142–H154.
- (49) Lyons, M. E. G.; Brandon, M. P. The Oxygen Evolution Reaction on Passive Oxide Covered Transition Metal Electrodes in Alkaline Solution. Part III - Iron. *Int. J. Electrochem. Sci.* **2008**, *3*, 1463–1503.
- (50) Takashima, T.; Hashimoto, K.; Nakamura, R. Mechanisms of pH-Dependent Activity for Water Oxidation to Molecular Oxygen by MnO<sub>2</sub> Electrocatalyst. *J. Am. Chem. Soc.* **2012**, *134*, 1519–1527.
- (51) Lyons, M. E. G.; Doyle, R. L.; Godwin, I.; O'Brien, M.; Russell, L. Hydrous Nickel Oxide: Redox Switching and the Oxygen Evolution Reaction in Aqueous Alkaline Solution. *J. Electrochem. Soc.* **2012**, *159*, H932–H944.
- (52) Yeo, B. S.; Bell, A. T. In Situ Raman Study of Nickel Oxide and Gold-Supported Nickel Oxide Catalysts for the Electrochemical Evolution of Oxygen. *J. Phys. Chem. C* **2012**, *116*, 8394–8400.
- (53) Bandaru, P. R. Electrical Properties and Applications of Carbon Nanotube Structures. *J. Nanosci. Nanotechnol.* **2007**, *7*, 1239–1267.
- (54) Hersam, M. C. Progress Towards Monodisperse Single-Walled Carbon Nanotubes. *Nat. Nano* **2008**, *3*, 387–394.
- (55) Liu, H.; Feng, Y.; Tanaka, T.; Urabe, Y.; Kataura, H. Diameter-Selective Metal/Semiconductor Separation of Single-wall Carbon Nanotubes by Agarose Gel. *J. Phys. Chem. C* **2010**, *114*, 9270–9276.